

FEMME: A multi-scale Finite Element Microstructure MESHfree fracture model for quasi-brittle materials with complex microstructures



Luis Saucedo-Mora^a, T. James Marrow^{a,b,*}

^a University of Oxford, Department of Materials, Parks Road, Oxford OX1 3PH, United Kingdom

^b University of Oxford, Oxford Martin School, Parks Road, Oxford OX1 3PH, United Kingdom

ARTICLE INFO

Article history:

Received 17 December 2014

Received in revised form 15 May 2015

Accepted 28 May 2015

Available online 4 June 2015

Keywords:

Multi-scale model

FEM, Meshfree

Microstructure

Quasi-brittle fracture

ABSTRACT

In this paper we develop a very efficient Finite Element Microstructure MESHfree (FEMME) method to account for the effect of microstructure on quasi-brittle properties within finite element simulations of damage, improving the accuracy and computational cost of calculations at engineering length-scales. This method provides two sets or layers of elements representing the Finite Element Model and the microstructure. The first is used to link the engineering scale problem with the microstructure, obtaining the stress and strain fields of the macro-mechanical problem; from these, we compute the micro-mechanical fields using the second set of elements, which describes explicitly the microstructure.

© 2015 The Authors. Published by Elsevier Ltd. This is an open access article under the CC BY license (<http://creativecommons.org/licenses/by/4.0/>).

1. Introduction

One of the main problems in numerical models is scale. If the microstructure is inserted in the model with a high fidelity, the computational cost grows; this makes the application of microstructure-sensitive models at engineering length scales difficult. Accordingly, to model a full-scale component while reducing the computational cost to a currently feasible level, a simplified model is used. One simplification is the use of a continuous material instead of a complex microstructure, and a coarse discretization compared with the microstructural scale, which is called a Representative Volume Element (RVE); this epitomises the length scale over which microstructure provides homogeneous properties. Consequently, the Finite Element Model (FEM) needs to use a large mesh size. In inelastic materials, such as quasi-brittle materials, the use of a coarse mesh results in a significant overestimate of the strain energy release of the component with fracture, and consequently a solution that may be far from its real behavior. This mesh-size effect of cohesive element models has been reported widely in the literature. Carpinteri and Colombo [29] argue that when the structure is very large or the fracture toughness very small, the cohesive zone at the crack tip becomes relatively small compared with the size of the structure, so the mesh needs to be refined to ensure that the cohesive forces are closer from each other, otherwise the cohesive model is unable to describe the fracture process regularly. Möes and Belytschko [30] also show that in cohesive models the density of elements needs to be of at least 10 elements per characteristic length of the material (l_{ch}) in the crack path in order to obtain a representative result. This density can be decreased to 2 elements per characteristic length (l_{ch}) in XFEM approaches. Examples of quasi-brittle materials include cements and concrete [1], ceramic matrix composites [18] and polygranular

* Corresponding author at: University of Oxford, Department of Materials, Parks Road, Oxford OX1 3PH, United Kingdom.

E-mail address: james.marrow@materials.ox.ac.uk (T.J. Marrow).

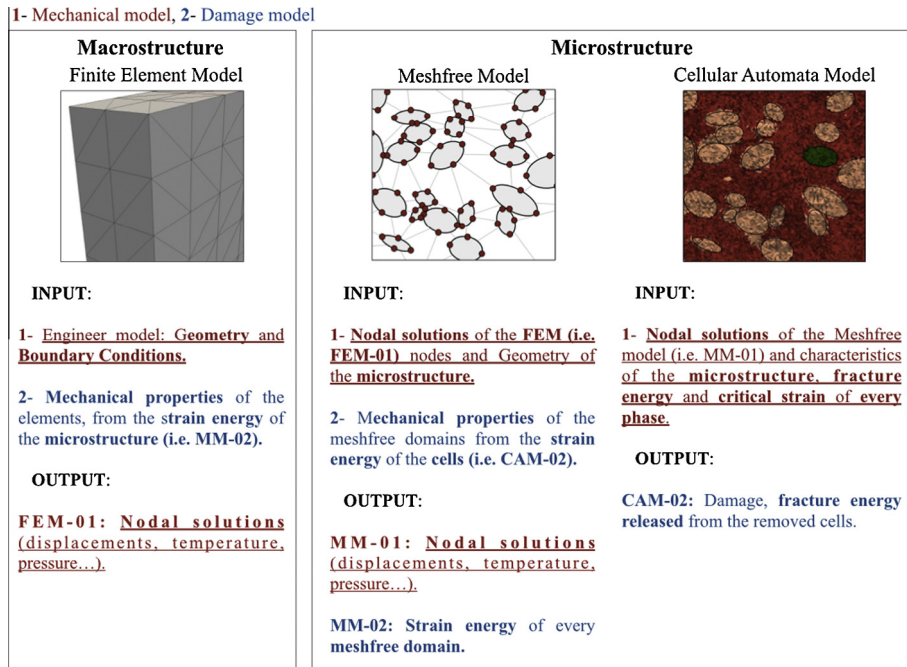


Fig. 1. Interaction between the layers of the FEMME model.

nuclear graphite [26]. In this work we propose a novel multi-scale solution that releases the spurious strain energy of a coarse mesh by introducing the microstructure as a local enrichment in the damaged zone. We insert all the material properties through the microstructural description of the quasi-brittle material, and achieve computational efficiency.

There are many fracture models in the literature that deal with quasi-brittle fracture through the use of a cohesive law. These models simplify the material as a continuum; the appearance of the crack within an element is represented either by a change in its mechanical properties, or the crack is represented at the interface of two elements by mesh splitting and inserting equivalent forces [2]. Such techniques include: cohesive element models [3], which insert homogeneous damage inside a FE; the Strong Discontinuity Approaches, which are evolutions of the cohesive elements method that inserts an oriented crack inside a FE; or the Cohesive Faces model [4], which inserts the crack at the interface of two elements. All these models use a fixed FE mesh during the calculation; the significant mesh sensitivity of the fracture process therefore needs to be addressed by using fine meshes or predefining the fracture path. Some models deal with this drawback through adaptation of the mesh during the fracture process; these enrichment methods include XFEM and EFEM [5]. All these methodologies share a continuum definition of the material used, which is quite different from the nature of quasi-brittle materials; these have complex microstructures that can exhibit considerable heterogeneity of microstructure and properties.

There is another class of numerical fracture models, which instead of assuming the material as a continuum, insert its microstructure explicitly to model the fracture. These models generally have a higher computational cost because they are multi-scale models that are composed from a series of sub-models, each dealing with one scale of the problem [6]. The cost can be reduced drastically through local insertion of the different layers. Examples of multi-scale models include the CAFE model [7]; a combination of a standard FE model for the large-scale model and a Cellular Automata model for the microstructure, and the PERMIX model [8], which uses FEM and XFEM at the different scales.

In this paper we present an approach based on a Finite Element Model with a coarse mesh normalizing the energy release by the joint application of two modeling approaches, a Meshfree Method and Cellular Automata; this achieves a significant reduction in computational cost. The Finite Element Microstructure Meshfree model proposed (FEMME) is not developed inside a single Finite Element, instead a continuum Meshfree model is developed inside a set that is composed of those elements that may develop damage. Through the adaptation of the Meshfree model to the microstructure, and also the cells that carry all the material properties and the damage information of the different phases of the material, the development of damage in a quasi-brittle material formed by a matrix and phases of different brittle properties can be simulated with high fidelity and low computational cost. The minimum size of the Finite Elements is not restricted, as in the RVE techniques, due to a homogenization of the material properties capable to introduce the heterogeneity of the material at this scale.

This paper presents the FEMME model, which uses the subdivision algorithm to insert a microstructure into a unstructured tetrahedral FE mesh presented by Saucedo-Mora and Marrow [9]. This is also applied independently to a fiber composite [18] and a Thermal Barrier Coating [19].

The paper is structured as follows: in Section 2 a description of the model and the interaction between the different layers is provided; Section 3 compares the strains obtained with the FEMME model and a high fidelity FEM in a complex microstructure; in Section 4 we present an example of the energy release normalization, comparing the FEMME model against a FEM with cohesive elements, in Section 5 the FEMME model is applied to the size effect in concrete beams; and in Section 6 the FEMME model is compared with other methodologies, including XFEM, in terms of computational cost and accuracy.

2. Mechanical model

A general CAFE method was first presented by Shterenlikht and Howards [7], but in order to adapt this methodology to our requirements we insert variations in its discretization and the relationship between the CA and FE layers. This results in the FEMME (Finite Element Microstructure MESHfree) methodology proposed here that consists of 3 layers, each one represented by a different mechanical model and linked with the others through energy homogenization. FEM is used for the macromechanical model, a Meshfree model to compute the displacements of the microstructural features and CA to reproduce the fracture properties of the different phases.

Fig. 1 explains the FEMME model schematically, showing the inputs and outputs of every layer used. The FEM carries all the geometrical information of the engineering scale component, as well as its boundary conditions and bulk mechanical properties of the different materials, which will change with the damage that is described by the strain energy of its microstructure (represented by the Meshfree domains). In each iteration, after running the FEM, its nodal solutions (i.e. displacements or temperature) are used as inputs of the Meshfree model that calculates the movements of the microstructural features. The Meshfree model also needs the geometrical description of the microstructure features and their mechanical properties, which are related to the strain energy of the materials in the Cell layer. The nodal solutions of the Meshfree model are used as an input to the CA model to calculate the strains of the cells; any cell is removed if its critical strain is exceeded. After computing the damage in the cells, the strain energy of the Meshfree domains is recomputed considering the fracture energy released by the damaged cells, then the mechanical properties of the Meshfree domains are recalculated. Finally the mechanical properties of the Finite Elements are recomputed considering the strain energy of the Meshfree domains.

2.1. Subdivision algorithm and Cellular Automata representation of microstructure

To ensure the versatility of our method we work with an irregular tetrahedral mesh, which increases the complexity of the subdivision process. To address this, an iterative algorithm is developed [9]; each tetrahedron of the FE model is subdivided into 4 similarly sized tetrahedrons through the use of a common vertex and dividing the opposite face into 4 triangles that are defined by the midpoints of its edges. In order to create cells that are as regular as possible, the largest area face of the tetrahedron is chosen for division. This process is iterated until the mean cell volume is representative of the microstructural size. The total number of cells inside an element is 4^n , n being the number of iterations. Once we have the set of cells, we identify those within ellipsoids of various sizes and orientations that represent different phases in a matrix, such as pores and particles. In that way, the cells reproduce the volume and proportion of the different phases of the microstructure; it is also possible to insert straight and curved fibers, see Saucedo and Marrow [9,10]. With sufficient subdivision, the initial FE mesh has no effect on the cellular description of the microstructure.

2.2. Finite Element model

The Finite Element part of the model is implemented within the software ABAQUS 6.10. For this we use a variation of the cohesive element, but instead of following a cohesive law, it receives from the microstructure information of the energy released in the fracture through homogenization [11], which is used to update the mechanical response of the element. We use a tetrahedral mesh with a single integration point.

2.3. Meshfree model

This layer is the link between the information of the Finite Element Method and the Cellular Automata through a Microstructural Adaptive Meshfree framework (MAM). Once distributions of the ellipsoids that represent pores and particles are described (we represent a pore as an empty particle), we carry out a Delaunay triangularization [12] to define the Inter Particle Domains (IPD). The Particle Domains (PD) are defined by the interior of each ellipsoid; these are part of the discretization of the Meshfree model with the particles. There are two ways to discretize the particles: one is to insert one node in the intersection of every edge of the tetrahedrons that form the IPDs around the particle, with a variable total number of nodes per particle between 8 and 20; the other discretization possible is assigning a constant number of nodes per particle, e.g. 6 nodes by considering one at each end of the principal axis of the ellipsoid.

Fig. 2 shows the local stiffness matrix $[K]$ computed for the 2 possible discretizations. On (a) 12 nodes are used to discretize the particle, and on (b) 6. The local stiffness matrix of the particle in both cases is computed using the same shape function (Eqs. (6) and (7)). The figure shows that the matrix of the particle with 6 nodes is better conditioned; this avoids instability because of its more dominant diagonal, which may be because both are calculated with the influence of the same number of IPDs. To construct a mechanical model with the discretization of 6 nodes per particle we need a flexible shape

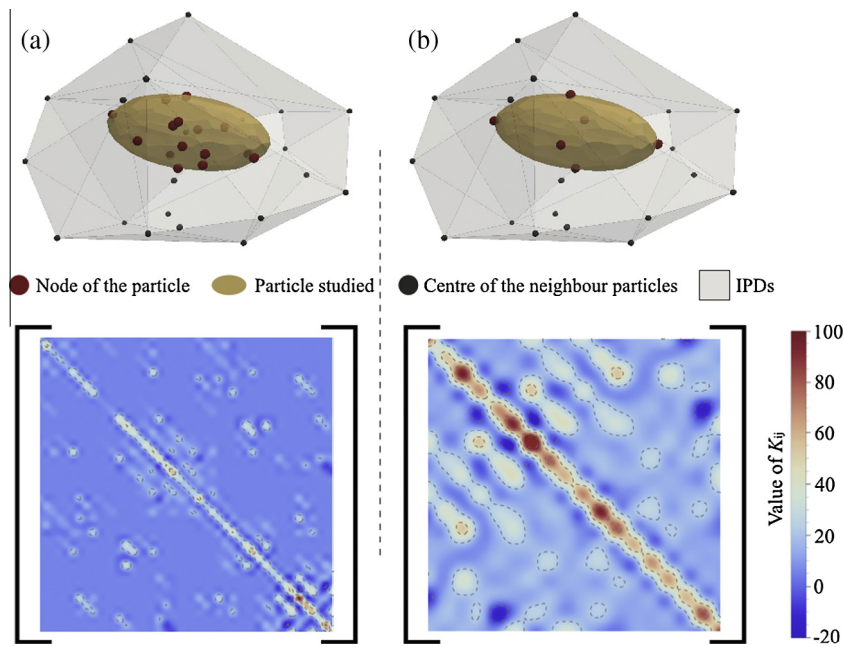


Fig. 2. Local stiffness matrix for the different discretization of the particles. (a) The particle discretized with 12 nodes, and (b) with 6.

function that enables us to deal with complex domains (i.e. from each of the 4 particles that defines the IPD, the 3 nodes closest to the center of the domain). For this reason, and to ensure the stability of the microstructural adaptive model, a meshfree approach is used.

In addition to the main pores or particles, micropores (i.e. spherical pores with a small radius) are inserted in the particle set before the Delaunay triangularization in order to increase the discretization of the Meshfree model; these do not affect the fracture behavior themselves. 6 points represent each ellipsoid, with one at each end of its orthogonal axes. Each IPD is composed by 4 ellipsoids and 12 nodes and is defined by the 3 nodes of these that are closest to the IPD center. Consequently, in the Meshfree Model we have two different types of domains: IPD with 12 nodes that represent the matrix, and PD with 6 nodes in the interior of each ellipsoid (Fig. 3). The versatility of the Meshfree model allows us to have variable domains with different geometries and number of nodes. For this we enforce the local maximum entropy conditions described by Arroyo and Ortiz [13] and the geometrical adaptive conditions of Saucedo-Mora [14].

Currently, the microstructure is created through the definition of the IPDs and PDs at the beginning of the model, being inactive initially and becoming part of the MAM model once they are active. A further development planned will lead to local creation of the microstructure directly inside the damaged elements doing a Delaunay triangularization at every step; the advantage of this is the higher efficiency due to the lower amount of information predefined. Inside every Finite Element

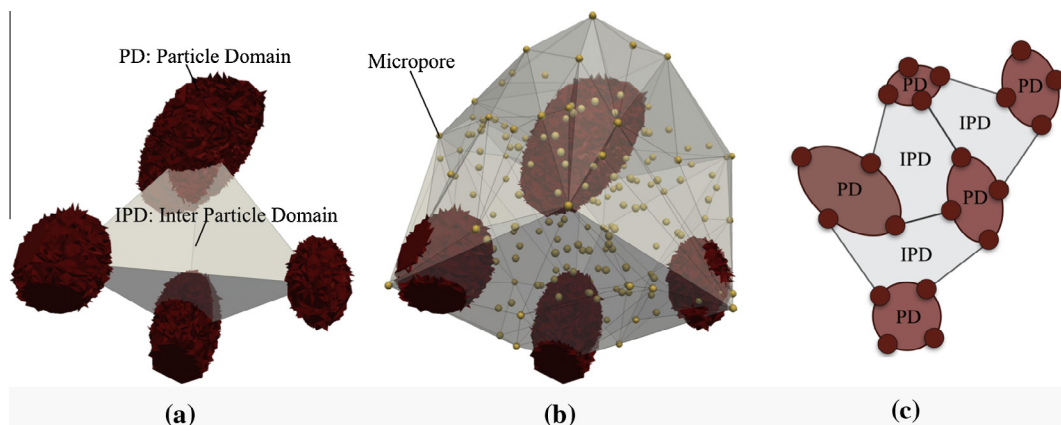


Fig. 3. Domains of the MAM framework; (a) 3D view of the Inter Particle Domains (IPD) and Particle Domains (PD); (b) enrichment with micropores to increase the discretization; (c) 2D scheme of the discretization.

there are IPDs and PDs that became active when the element reaches a state sufficient to generate damage. Currently, we apply a stress criterion, such that damage may occur when the stress has a value of $0.5f_t$, where f_t is the representative tensile stress of the material. This is argued in point 4 where the influence of this coefficient where the FE is subdivided is evaluated. Within each IPD and PD, the cells determine the material properties as damage develops.

The damaged domains of the FE mesh are occupied by the Meshfree domains of the next layer. This two domains are not exactly related through shape, since the geometries of the FE mesh and Meshfree discretization are determined respectively by the shape of the large scale component and the microstructural features. This causes a difference between the volume of the FE and the sum of the volumes of the IPDs and PDs inside it. The volume of the IPD and PD with nodes outside of the host finite element needs to be corrected for the homogenization, which is done through its shape function; if a node is outside of the FE, its proportional volume is removed.

We consider, in Eq. (1), a Finite Element that is defined by a tetrahedron of nodes n_1, n_2, n_3, n_4 , and an arbitrary point evaluated n_{ev} ,

$$\sum_{a=1}^{a=4} \frac{V_{tetra}(face_a^e, n_{ev})}{V_{tetra}^e} = 1 \quad face^e = \{(n_1, n_2, n_3), (n_1, n_2, n_4), (n_1, n_3, n_4), (n_2, n_3, n_4)\} \quad (1)$$

where $face^e$ is the set composed by the faces of the tetrahedron evaluated (i.e. element of the FE mesh), and V_{tetra}^e its total volume. The function $V_{tetra}(face_a^e, n_{ev})$ computes the volume of the tetrahedron formed by the face selected and the point evaluated; the result of Eq. (1) is higher than 1 if the point n_{ev} is outside of the FE evaluated. With this we can evaluate whether a certain node is inside of the FE studied.

With the sets of nodes inside and outside a certain Finite Element known, we can correct the volume of the IPD or PD that are partially outside the FE using Eq. (2). This is important for the energy homogenization that is carried out between layers because the strain energy of the domain is incorrectly determined if there is not an agreement between both volumes; this would otherwise produce errors in the cohesive behavior of the damaged FE. The corrected volume is given by Eq. (2),

$$V_{MD}^1 = \sum_{i=0}^{i=m} N(\bar{x})^g|_i V_{MD}^0 \quad (2)$$

where MD is the Meshfree Domain evaluated (IPD or PD), m is the set of nodes of the MD inside the FE, V_{MD}^0 is the total volume of the Meshfree Domain and V_{MD}^1 is the corrected volume to be used in the energy homogenization.

The main difference between the Meshfree and the finite element layers is the shape function, which is more flexible and versatile for domains with complex geometries and domains with different number of nodes. This makes the Meshfree method suitable for a model that is adapted to a complex microstructure, creating different domains with a single integration point where the strains and stresses are computed. Due to the complexity of the Meshfree discretization, different exponential shape functions are used for the IPDs and the PDs; as for any shape function, the function needs to be positive and meet the partition of unity and interpolation conditions.

$$N(\bar{x})^a \geq 0 \quad \bar{x} = \{x_1, x_2, x_3\} \quad \forall x_i \in \Re \quad (3)$$

$$\sum_{a=0}^{a=n} N(\bar{x})^a|_g = \sum_{a=0}^{a=n} N(\bar{x})^g|_a = 1 \quad (4)$$

$$\sum_{a=0}^{a=n} N(\bar{x})^a|_g \mathbf{u}^a = \mathbf{u} \quad (5)$$

where g is the integration point of the domain, and a is the node evaluated. Because a Meshfree framework is used, the position of the integration point and the size of the domain are not directly determined. These need to be computed separately to allow the shape function to share equally the influence of every particle in the domain, ensuring that the sum of the derivatives is equal to zero in order to avoid spurious strains [15]. Those conditions are automatically fulfilled by the PDs by considering the center, size and orientation of the ellipsoid inserted to reproduce the particle [9], but the shape function needs to be computed separately for every IPD.

The general forms of the shape functions (Eqs. (10) and (11)) for the IPD and PD use the function S defined by Eqs. (6) and (7).

For the IPD

$$S(\bar{x}, \bar{x}^c, \bar{l}_D)^g = \text{Exp} \left[-\gamma_e \left(\left(\frac{x_1^c - x_1}{l_1} \right)^2 + \left(\frac{x_2^c - x_2}{l_2} \right)^2 + \left(\frac{x_3^c - x_3}{l_3} \right)^2 \right) \right] \quad (6)$$

where l_1, l_2 and l_3 are the maximum distances in the 3 spatial axes between the center of the IPD and its nodes.

For the PD

$$S(\bar{x}, \bar{x}^c, \bar{l}_D, \bar{\alpha})^g = \text{Exp} \left[-\gamma_e \left(\left(\frac{d_1}{l_1} \right)^2 + \left(\frac{d_2}{l_2} \right)^2 + \left(\frac{d_3}{l_3} \right)^2 \right) \right] \quad \bar{\alpha} = \{\alpha_1, \alpha_2, \alpha_3\} \quad (7)$$

This shape function uses the geometry of the particle that it represents, which is oriented in 3D and has different dimensions in each of its axes.

$$[A] = \begin{pmatrix} 1 & 0 & 0 \\ 0 & \cos(\alpha_1) & \sin(\alpha_1) \\ 0 & -\sin(\alpha_1) & \cos(\alpha_1) \end{pmatrix} \begin{pmatrix} \cos(\alpha_2) & 0 & -\sin(\alpha_2) \\ 0 & 1 & 0 \\ \sin(\alpha_2) & 0 & \cos(\alpha_2) \end{pmatrix} \begin{pmatrix} \cos(\alpha_3) & \sin(\alpha_3) & 0 \\ -\sin(\alpha_3) & \cos(\alpha_3) & 0 \\ 0 & 0 & 1 \end{pmatrix} \quad (8)$$

$$\begin{pmatrix} d_1 \\ d_2 \\ d_3 \end{pmatrix} = [A] \begin{pmatrix} x_1^c - x_1 \\ x_2^c - x_2 \\ x_3^c - x_3 \end{pmatrix} \quad (9)$$

where $\alpha_1, \alpha_2, \alpha_3$ are respectively the pitch, roll and yaw Euler angles, the vector \bar{x}^c is the position of the integration point which is the center of the domain, and the vector \bar{x} is the generic point evaluated. The constant γ_e is an arbitrary parameter to improve the performance of the shape function [13]. Here we have assumed $\gamma_e = 0.5$ because of the complexity of the domains, which ensures an influence of the nodes far from the center of the IPD or PD. With this we rotate the shape function to ensure that it is coupled with the particle's geometry. In that case the Euler angles are those of the particle, which has been inserted randomly in the microstructure [9]. If it is desired to reproduce faithfully a specific particle orientation, Slabaugh's formulation [16] can be used to compute these angles.

The general form of the shape function is:

For the IPD

$$N(\bar{x})^g = S(\bar{x}, \bar{x}^c, \bar{l}_D)^g / \sum_{i=1}^{i=n} S(\bar{x}, \bar{x}^c, \bar{l}_D)^g \quad (10)$$

For the PD

$$N(\bar{x})^g = S(\bar{x}, \bar{x}^c, \bar{l}_D, \bar{\alpha})^g / \sum_{i=1}^{i=n} S(\bar{x}, \bar{x}^c, \bar{l}_D, \bar{\alpha})^g \quad (11)$$

The shape functions defined by Eqs. (10) and (11) meet the general requirements established in Eqs. 3–5, and are applied independently inside each Meshfree Domain with Kronecker's delta property [17].

The shape function itself is used to interpolate the results of the Meshfree nodes (i.e. displacements [18] or temperature [19]) and to create the data field of the Cellular Automata layer. To create the stiffness matrix of the Meshfree problem, used to compute the strains of its domains, the derivatives of the shape functions are needed; Eqs. (12) and (13) show the derivatives of the shape function for the different Meshfree domains.

$$\frac{\partial N(\bar{x})^g}{\partial x_i} = -\gamma_{d_{ipd}} 2 \frac{(x_i^c - x_i)}{l_i} N(\bar{x})^g \quad \forall i = 1, 2, 3 \quad (12)$$

$$\frac{\partial N(\bar{x})^g}{\partial x_i} = -\gamma_{d_{pd}} \frac{\partial \left((d_1/l_1)^2 + (d_2/l_2)^2 + (d_3/l_3)^2 \right)}{\partial x_i} N(\bar{x})^g \quad \forall i = 1, 2, 3 \quad (13)$$

Here the values of γ_d used are 3 for the IPDs (Eq. (25)), and 1.5 for the PDs in order to ensure that the shape functions represent the different discretizations of 12 (IPD) and 6 (PD) nodes. Those derivatives are used to compute the strains of the Meshfree domains with Eqs. (14) and (15).

$$\varepsilon_{ij}^g = \frac{1}{2} \sum_{a=0}^{a=n} \left[(\nabla N(\bar{x})^a|_g)_j \bar{u}_i + (\nabla N(\bar{x})^a|_g)_i \bar{u}_j \right] \quad (14)$$

$$\varepsilon_{ii}^g = \sum_{a=0}^{a=n} \left[(\nabla N(\bar{x})^a|_g)_i \bar{u}_i^a \right] \quad (15)$$

$$\bar{\varepsilon}^g = [B] \bar{u}_i^a \quad (16)$$

With the sum of Eqs. (14) and (15) we can determine the $[B]$ matrix of Eq. (16), which is used in Eq. (17) to compute the equilibrium of forces.

$$\bar{f}_D = V_D [B_{Loc}]^T [D]_D [B_{Loc}] \bar{u}_D \quad (17)$$

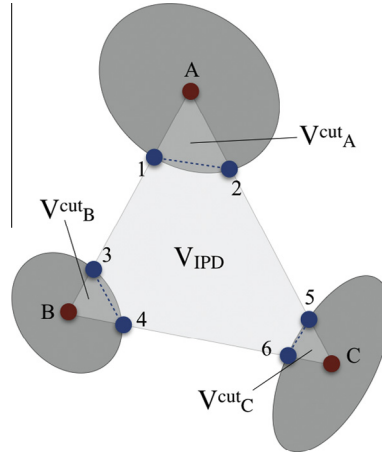


Fig. 4. Volume of an IPD truncated by the PDs at its vertex.

where V_D is the volume of the IPD or PD evaluated, which needs to be calculated. After this, Eq. (17) needs to be assembled into the global stiffness matrix. The calculation of the volume of each Meshfree domain is studied from Eqs. (18)–(22).

For the PD

$$V_{PD} = \pi \frac{4}{3} l_1 l_2 l_3 \quad (18)$$

The volume of the Particle Domains is calculated using the size of the ellipsoid that defines the particle studied, and the analytical solution of its volume.

For the IPD

The Inter Particle Domains are truncated tetrahedrons with vertices cut by the elliptical particles of the domain (see Fig. 4). The true surface that truncates each vertex is curved, but for simplicity we use a plane formed by the crossing points between the tetrahedron and the ellipse studied. With Eqs. (19)–(21) we compute the intersection between the segment defined by the center of two particles (i.e. AB, AC, BC in Fig. 2) and that of each ellipsoid. As an example, first we define the parametric segment between A and B with Eq. (19), and evaluate each point of this segment changing t until Eq. (21), which defines the surface of the ellipsoid, is satisfied; t ranges from 0 to 1 and can be computed with the bisection method. With this, combining the segment AB with the particle A, we compute point 1, and with the same methodology we compute the remaining points shown in Fig. 4; these define the truncated vertices of the tetrahedron, and the corrected volume can be computed using Eq. (22).

$$\bar{x}(t) = \bar{x}^A + t(\bar{x}^B - \bar{x}^A) \quad t \in [0, 1] \quad (19)$$

$$\bar{d} = [A](\bar{x}^C - \bar{x}(t)) \quad (20)$$

$$\frac{d_1^2}{l_1^2} + \frac{d_2^2}{l_2^2} + \frac{d_3^2}{l_3^2} = \text{Log}[\gamma_e] \quad (21)$$

With this we compute the 3 crossing points between each particle and the tetrahedron formed by the centers of the 4 particles of the IPD (see Fig. 4 for a 2D scheme). Those points define the subtetrahedrons (i.e. A-1-2, C-5-6 and B-3-4 in Fig. 4) whose volumes need to be subtracted from the main tetrahedron of the IPD.

The corrected volume of the IPD to be used in Eq. (17) is:

$$V_{IPD} = V_T - \sum_{i=0}^{i=4} V_i^{\text{Cut}} \quad (22)$$

V_{IPD} is the corrected volume of the IPD, V_T the original volume of the tetrahedron formed by the centers of the particles, and V_i^{Cut} is the truncated volume of each vertex.

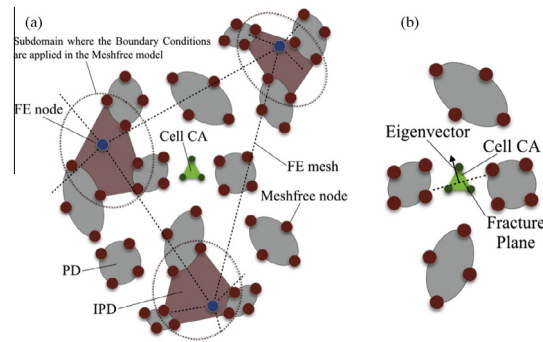


Fig. 5. Three layers together and its relationships; (a) FE mesh with its nodes, the Meshfree nodes and domains where the boundary conditions are applied and a cell of the CA layer; (b) the insertion in a damaged CA of the local fracture plane orthogonal to the eigenvector associated with the principal maximum strain.

2.4. Boundary conditions

The boundary conditions play an important role in the model. The inputs of the Meshfree model from the FE are the nodal displacements of the FE mesh. These are inserted in the IPD that encloses each node (Fig. 5a). Once the Meshfree model is computed, the displacements of the Meshfree nodes are mapped into the nodes of the CA model to compute the increment of the cell's strain and updated using the MAM nodes at the same side of the fracture plane (i.e. plane orthogonal to the maximum principal strain eigenvector) if the cell is removed (Fig. 5b). The displacements of the CA model are interpolated using the shape functions of each IPD or Particle.

2.5. Displacements of the CA layer

The displacements of the microstructural features are mapped into the nodes of the cells in the CA layer through the Meshfree shape function shown in Eqs. (10) and (11), using the interpolation described in Eq. (5). Here we need to differentiate between the interpolation of the displacements in the non-damaged and damaged cells. In the case of a non-damaged cell, all the nodes of the Meshfree domain that contains the cell evaluated are used. For the nodes of a damaged cell, only the Meshfree nodes at its same side of the local fracture plane are considered for the interpolation, updating this way the nodes of a damaged cell in both sides of the local fracture plane; this has the effect of addressing the increased local compliance and strain concentration arising from a crack-like defect. The fracture plane of the cell is determined as the plane that crosses the center of the cell and is orthogonal to the eigenvector that is related to the maximum principal strain. Once we have interpolated the displacements of every cell we compute its strain as a sum of the strain of the Meshfree domain (ε_{kl}^{MD}) that contains the cell, using Eq. (23).

$$\varepsilon_{kl} = \varepsilon_{kl}^{MD} + \frac{1}{12} \sum_{i=0}^{i=4} \sum_{j=i+1}^{j=4} \left[\frac{u_k^i - u_k^j}{x_l^i - x_l^j} + \frac{u_l^i - u_l^j}{x_k^i - x_k^j} \right] \quad (23)$$

where j and i are the different nodes of the cell evaluated, this strain being the average of the strains between the nodes of the cell.

2.6. Erosion (i.e. damage)

The strain of every cell, computed using Eq. (23), is evaluated against its critical strain. The critical strain of the each cell is assigned using data that can be extracted either from a lower scale model or mechanical testing at an appropriate length scale (e.g. micromechanical tests). If the critical strain is reached, the cell is removed (i.e. eroded), and the displacements of the nodes of that cell are updated. As described in Section 2.5, in order to reproduce the strain intensification that caused by crack-like defects, the nodal displacements are updated by considering only the Meshfree nodes that are on the same side of the local plane that is orthogonal to the principal eigenvector of the damaged cell. This changes the strains of the cells in the neighborhood and allows the fracture to propagate in a crack-like manner as the model reproduces the strain concentration on the crack tip; an example of fracture propagating between two pores within a finite element is shown in Fig. 6. Due to the Meshfree method, if the propagating damage encounters the surface of the Finite Element that contains it, the damage crosses the interface of the FE (Fig. 7), damaging the nearest cell of the neighboring element and updating the displacements accordingly.

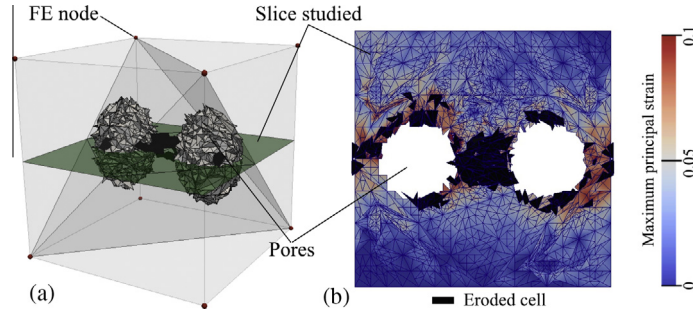


Fig. 6. Simulation of the strain concentration effect for damage between two pores: (a) view of the FE, the pores and the damaged cells; (b) detail within a 2D slice of the 3D finite element of the strain concentration effect generated by the damaged cells.

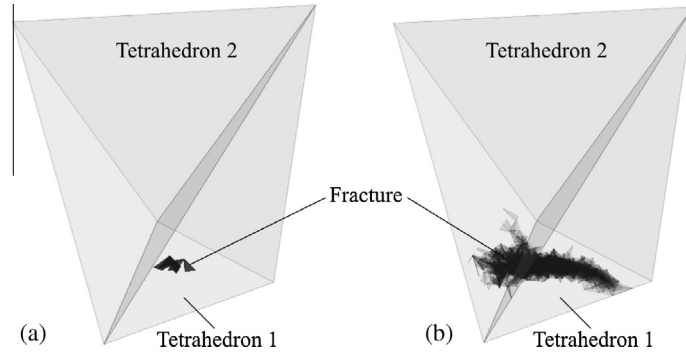


Fig. 7. Example of propagation of fracture across the interface of two finite elements defined by Tetrahedron 1 and Tetrahedron 2.

2.7. Energy homogenization

Energy homogenization links the effects of the eroded cells and the FE behavior [11]. For this, the strain energy of every IPD or PD at the beginning of the step is corrected with the energy released by every cell eroded inside each Meshfree domain (Eq. (25)), thereby changing the material properties of the IPD or PD accordingly by recalculating $[D]_{new}$. This is carried out similarly between the FE and Meshfree layer (Eq. (26)), changing the stiffness of the FE proportionally to the sum of the strain energy of all the enclosed IPDs and PDs and the strain of the FE at the beginning of the step, hence recalculating its $[D]_{new}$ matrix. Consequently, the damage at the microstructure lengthscale is translated from the CA layer to the FEM in a consistent way.

$$U_{cell(eroded)} = 0 \quad (24)$$

$$U_{IPD \text{ or } PD} = \sum_{i=0}^{i=n} U_{cell_n} = (Vol \cdot ([D]_{new} \cdot \bar{\epsilon}) \cdot \bar{\epsilon})_{IPD \text{ or } PD} \quad (25)$$

$$U_{FE} = \sum_{i=0}^{i=m} U_{IPD_m} + \sum_{i=0}^{i=l} U_{PD_l} = (Vol \cdot ([D]_{new} \cdot \bar{\epsilon}) \cdot \bar{\epsilon})_{FE} \quad (26)$$

3. Validation A: The effect of particle stiffness on the strain fields obtained by FEMME and FEM

This validation example of the FEMME model considers a cube of 1x1x1 mm, which contains 70 particles and is defined by 5 tetrahedron elements (Fig. 8b). It is embedded into a larger Finite Element Model (FEM) (Fig. 8a) composed by 135 elements and 700 particles. This method of embedding in a larger FEM is used to ensure that the boundary conditions applied to the FEMME volume are close to those of the equivalent volume of the validation model with a finely meshed FEM of the same microstructure; this is needed as the boundary condition displacements are applied only to the nodes of the coarse mesh of FEMME. Iterative subdivision of the 5 elements inside the cube produced 32,768 cells; the approximately equivalent resolution FEM has 40,000 tetrahedral elements, each with a single integration point and also embedded into a larger FE coarse

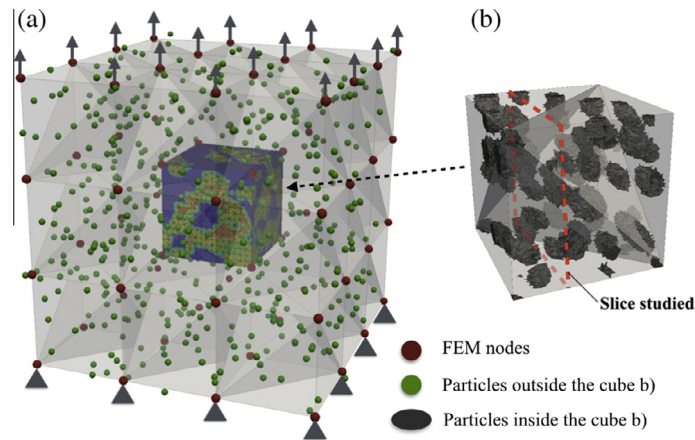


Fig. 8. Comparison of FEM and FEMME models; (a) full FEMME model used with the applied boundary conditions; (b) the microstructure and the 5 Finite Elements model (with 32,768 cells) used as a subvolume in the FEMME.

model. The arbitrary material properties are a Poisson's ratio of 0.2 and Young's moduli of 12 GPa for the matrix, 0 GPa for empty particles and 12,000 GPa for stiff particles. In the coarse FEM in which the microstructure volumes are embedded, a null displacement is applied to all the nodes of the bottom face, and a vertical displacement is applied to the top face to achieve a net strain of 0.06. In the general FEM used, the number of operations needed to solve the problem is proportional to the square of the number of nodes. With the FEMME model we reduce this number of operations, for an equivalent level of discretization between cells and FE elements, because the number of operations needed to compute the strains of the cells is linearly proportional to the number of cells, and those are only used locally in the damaged zones. To this we need to add the number of operations needed to solve the FEM and MAM layers of the FEMME model, which are proportional to the square of the number of nodes used; these are both very low due to the adaptability of the local MAM model and the coarse mesh used in the FEM. Considering this, in the example presented, the number of operations needed to solve the FEMME model is 2 orders of magnitude lower than that needed for the general FEM of the same microstructure with the same level of discretization. The achieved efficiency is especially important for fracture models where several iterations are required to allow the model to converge at every change in the boundary conditions.

The models were examined with the particles either as all pores (0 GPa), or all as stiff (12,000 GPa) relative to the matrix. The elastic strains obtained in the example of Fig. 8 are shown in Fig. 9 for the FEMME and FEM cases; the data are for a vertical section near the center of the cube, which is marked in Fig. 8b. The strains in this section are presented in Fig. 9a–f. Further detail is provided using example horizontal (Fig. 10a) and vertical (Fig. 10b) line profiles within this section, i.e. along the traces indicated by white lines of Fig. 7. The agreement between the two methods of the strain concentrating effect of the empty particles is quite acceptable, particularly in the magnitude of the strain concentrations close to the empty particles and the identification of the zones of higher and lower strains in the microstructure with stiff particles. For example, the zones with the higher and lower strains in the FEM are reproduced well by the FEMME model (Fig. 9b and e). These are the zones with a higher concentration of particles. These regions are larger in the FEMME model (Fig. 9a, b, d, and e), compared with the FEM analysis, due to the large size of the MAM domains. The strains of the cells are directly influenced by the strain of the MAM domain in which they are contained. This causes the wider range of higher strains in the FEMME model; there are zones with negligible strain at the borders of the modeled volume (in blue in Fig. 9a and d) – these occur as some of the cells in the border region are excluded from the calculation since they belong to MAM domains that are centered outside the cube studied. This effect is seen at the FEMME model edges in Fig. 10, and is also the reason why the MAM model has the shape that is shown in Fig. 9b and e. These effects would not occur in a larger model, and are essentially an artifact of the special case studied here, which has only 5 elements in the FEMME model.

It is noticeable that in the FEM the strains are more equally distributed, while in the FEMME the higher strains are concentrated around the empty particles, or in the matrix in the case with the stiff particles; these change the strains within zones that have different concentration of particles are due to conservation of the total strain energy of the volume. The FEM provides a more accurate description of the strain distribution than the FEMME, but the general pattern of strains in the microstructure is reproduced satisfactorily by the FEMME model, at a considerably lower computational cost. The agreement between the FEM and FEMME is best in the zones with higher strains where damage occurs, and it is consistent with the discretization level [9]. As a consequence, the FEMME approach is well suited to fracture calculations, as it is the strain concentrations that control damage.

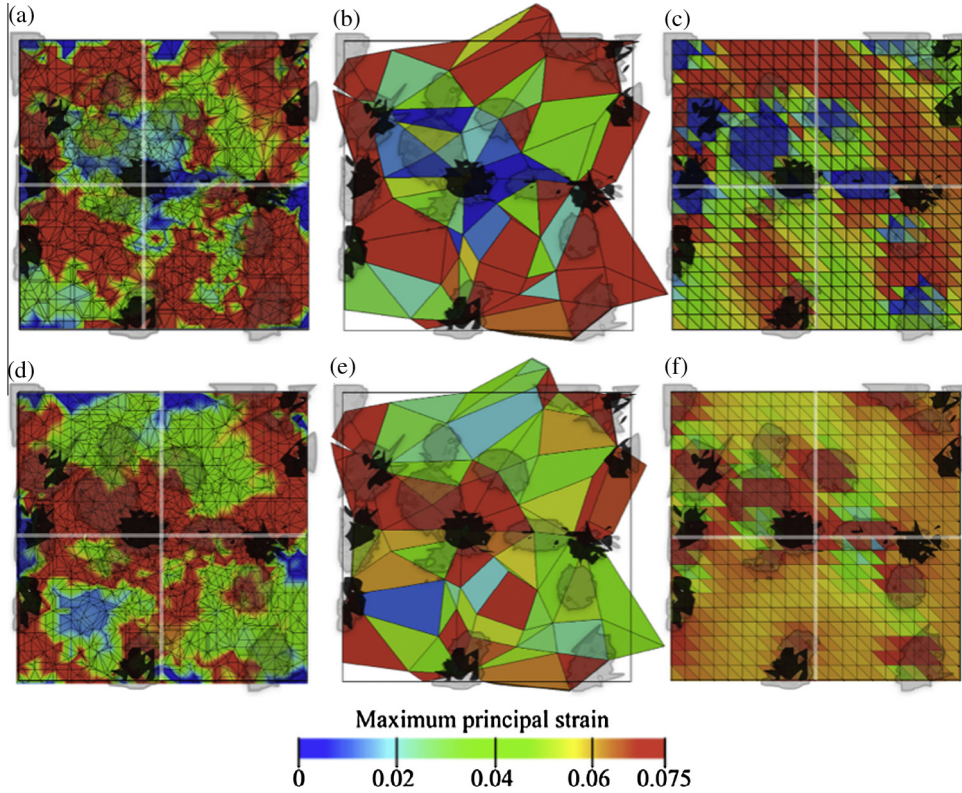


Fig. 9. Strains predicted in a vertical central slice by the 3D FEMME and FEM simulations at an equivalent level of discretization (from Fig. 8); Strains of the FEMME with stiff particles in the cells (a) and the IPD (b); (c) Strains of the FEM with stiff particles; Strains of the FEMME with empty particles in the cells (d) and the IPD (e); (f) Strains of the FEM with empty particles.

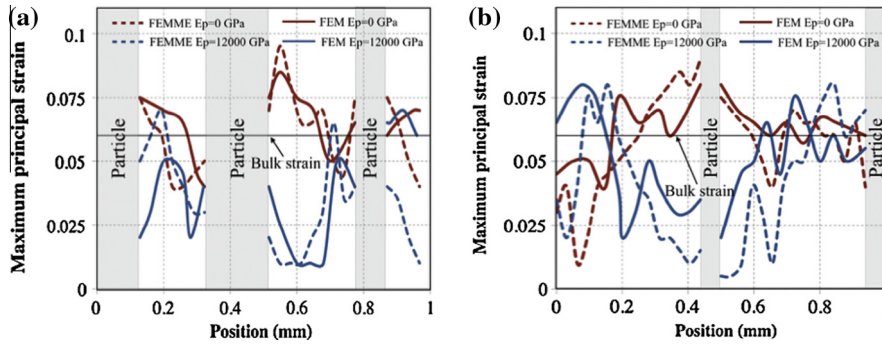


Fig. 10. Strains predicted in a vertical central slice by the 3D FEMME and FEM simulations at an equivalent level of discretization with empty particles ($E_p = 0$ GPa) and stiff particles ($E_p = 12,000$ GPa) (from Fig. 9); (a) strains along the horizontal and (b) vertical line profiles that are traced by the white lines in Fig. 9a, c, d, and f.

4. Validation B: The energy release in FEMME and FEM simulations of crack propagation

In this example we examine the strain energy release with damage propagation in a comparison of a FEM with cohesive elements against the FEMME model. The sample modeled is a $6 \times 6 \times 1$ mm rectangular prism under a vertical tensile load with two notches of 1 mm depth at different heights on opposite sides. The fictitious material has a Young's modulus of $E = 18$ GPa, a Poisson's ratio of 0.2 and a tensile strength of 3.3 MPa. In the FE, a linear decreasing cohesive law was defined for the cohesive elements, with a critical strain defined by the ratio between the tensile strength and the Young's modulus, and a constant final strain with zero tensile strength. In the FEMME model, the failure strain of each of the cells is defined randomly between the critical and final strains of the FE cohesive law, assigned with a linear probability distribution. The simulations of fracture initiation and propagation, and the microstructure description are independent with respect to

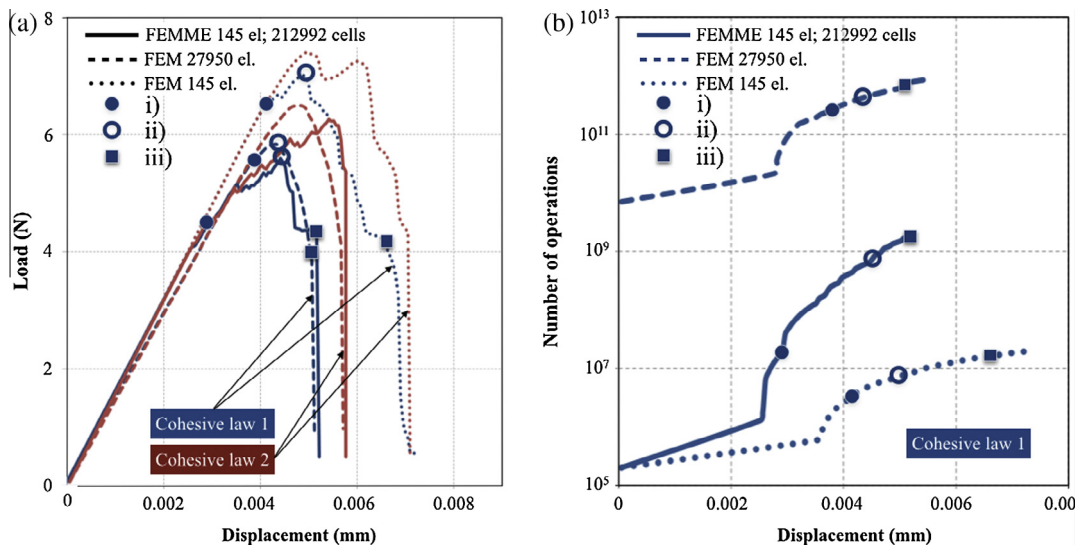


Fig. 11. Comparison between FEM and FEMME simulations of failure of a double-notched tensile specimen (see Fig. 11): (a) Load displacement curves for two example cohesive laws; (b) computational costs in term of operations for one cohesive law; In both figures the significant points of the calculations with the cohesive law 1 are marked with green circles: (i) damage initiation; (ii) peak load; (iii) collapse. (For interpretation of the references to colour in this figure legend, the reader is referred to the web version of this article.)

the mesh geometry, although the FEMME model does rely on the quality of the result given by the FE mesh. In particular, the FE mesh needs be sufficiently fine to reproduce the displacement field of the sample and to describe regions with strain intensity. Generally this can be achieved with a coarse mesh, except at regions such as stress concentrators where a finer mesh is required; in those cases the FEMME model can be easily coupled locally with cohesive elements to provide a good description of the displacement field.

The main result of this calculation is shown in Fig. 11a. This shows the difference between the FEM with coarse and fine meshes (145 and 27,950 elements respectively, and the FEMME model (based on the mesh of 145 elements, with 4702 IPD and 212,992 cells). Two cohesive laws have been considered: Cohesive Law 1 has a critical strain of 0.00018 and a final strain of 0.00055; Cohesive Law 2 has a critical strain of 0.00054 and a final strain of 0.00108. The FEMME model releases the spurious fracture energy of the coarse mesh, fitting the data of the fine mesh in both cases, showing the robustness of the method. The computational cost, which increases as damage develops, is shown in Fig. 11b; the FEMME is over an order of magnitude more efficient than the FEM of equivalent discretization, even in the later stages of damage propagation. The relationship between the discretization of the Meshfree model and two elements from the FE mesh is shown in Fig. 12a; the eroded cells are represented in Fig. 12b. The fracture pattern are visualized for the FEMs with coarse and fine mesh and the FEMME model at 3 different points in the simulations using Cohesive Law 1; the onset of non linearity, which is caused by damage initiation, the peak load and the final collapse; these points are marked in Fig. 11. The development of fracture is similar in the three models, showing the effects of the component geometry.

The total energy released during the fracture simulations with cohesive laws 1 and 2 is shown in Fig. 14a; that released by the FEMME method is equivalent to the fracture energy of the fine FE mesh, while the coarse FE gives an overestimate, as expected. The relation between stress and strain in the damaged elements is shown in Fig. 14b for both FEMME and the fine FEM (data for cohesive laws 1); the dashed red lines and the solid gray symbols describe the softening behavior of the finite elements that host the microstructural damage model in FEMME, and the solid red line is the cohesive law of the FEM; their softening behaviors are equivalent. The black dashed line is an exponential fit to the softening in the FEMME method and this is the cohesive law that emerges directly from the simulation of damage in the microstructure.

The size of the MAM discretization in the FEMME is fixed by the microstructure of the material, but the cell size within it can be arbitrary. To examine the sensitivity of the FEMME model to the discretization size, the double-notched specimen shown in Fig. 13 has been simulated with different numbers of cells per Meshfree domain. The results show an overestimation of the fracture energy and peak load (Fig. 15a) when the number of cells per Meshfree domain is lower than 20; the solution converges for higher values (Fig. 15b). This behavior arises from the role of the cells inside the Meshfree domain, which release its energy, and is independent of the material properties. If there are no cells inside a domain, this domain cannot be damaged, and we need at least, as an average, 20 cells per domain to guaranteed that every domain has cells inside and can be damaged efficiently.

The subdivision of the Fes at $0.5f_i$ is an arbitrary value to make the model local, which provides computational efficiency, and also to ensure that the subdivision takes place before the damage starts inside the FE; this avoids the artificial toughening of the material that would occur by subdividing the element after damage initiation. This is illustrated in Fig. 16.

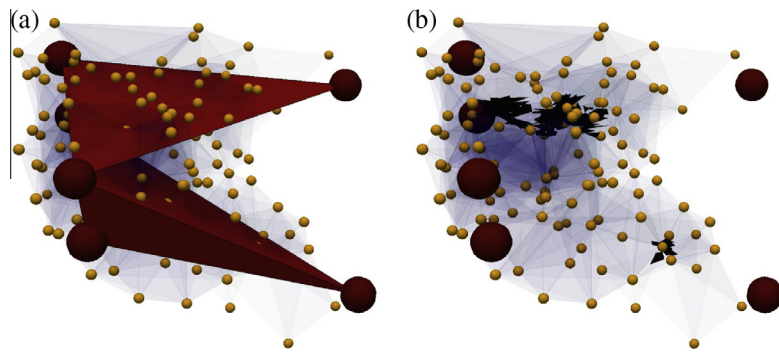


Fig. 12. Visualisation of the 3 length scales within the FEMME model: (a) the Meshfree model (IPD shown in blue and micropores in yellow) with the FE (element and nodes in shown in red); and (b) the CA (eroded cells shown in black). (For interpretation of the references to color in this figure legend, the reader is referred to the web version of this article.)

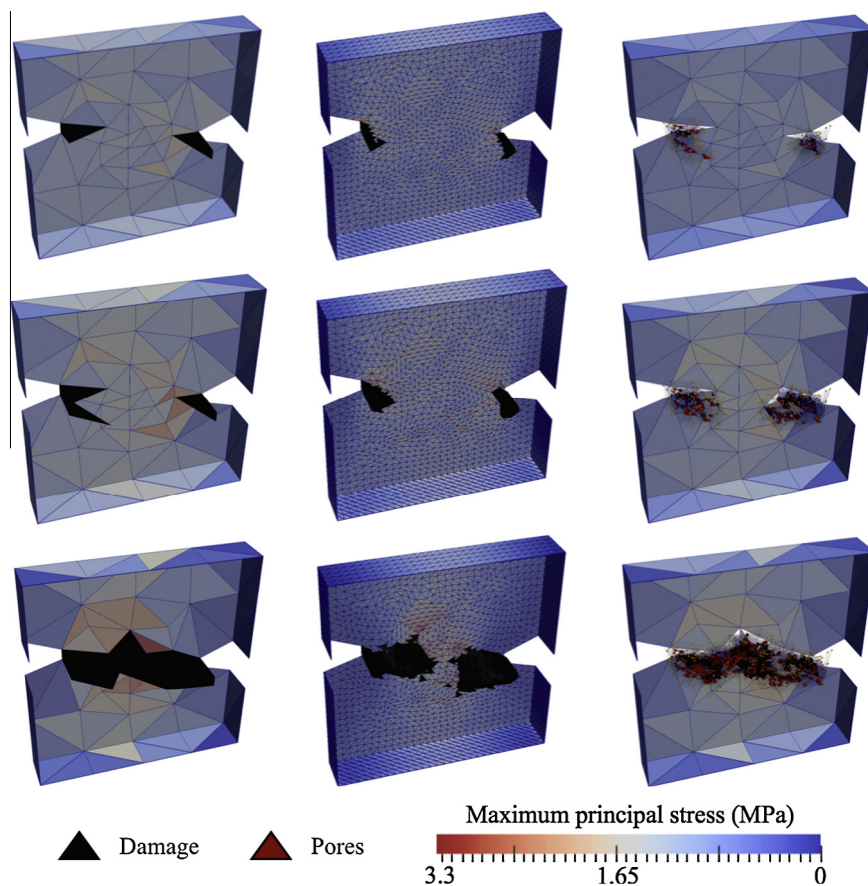


Fig. 13. Visualizations of the damage developed in the different models (for cohesive law 1): From top to bottom the fracture pattern at the onset of non linearity ('initiation'), the peak load and at collapse; From left to right the coarse FEM (145 elements), fine FEM (27,950 elements) and FEMME model (5 elements, 4702 IPD and 212,992 cells).

Fig. 16 shows that subdividing the FE before damage occurs within the element allows the model to reach a good solution. If the subdivision criteria is too high (e.g. in that case of subdivision at $0.9f_t$), there is artificial toughening. By reducing the criterion to below $0.7f_t$, the model converges to a solution. When we subdivide a FE we enrich the zone with the microstructure, and this increases the computational cost. The chosen criterion of $0.5f_t$ is conservative in terms of model precision; it could be increased to improve the computational cost.

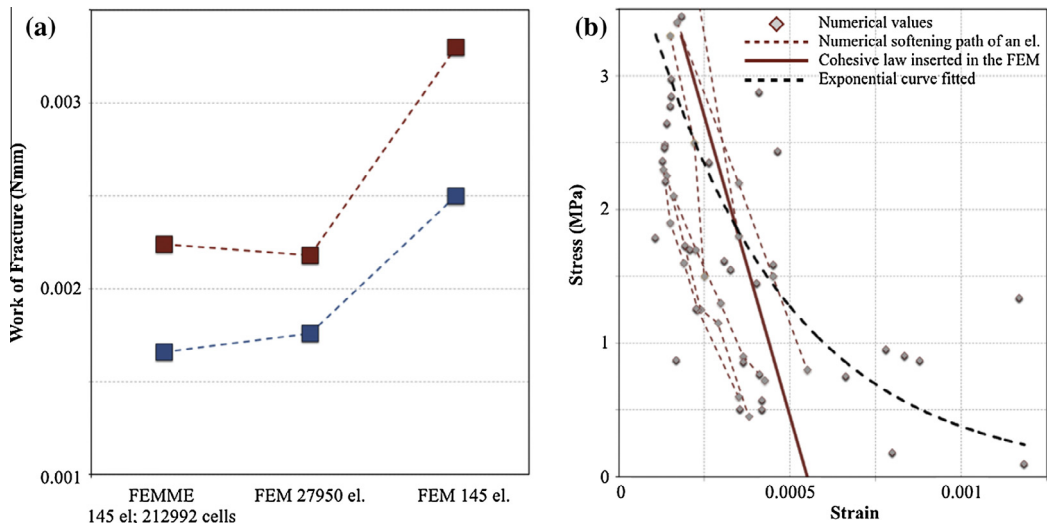


Fig. 14. Comparison between FEM and FEMM models of (a) Work of fracture and (b) the cohesive fracture behavior.

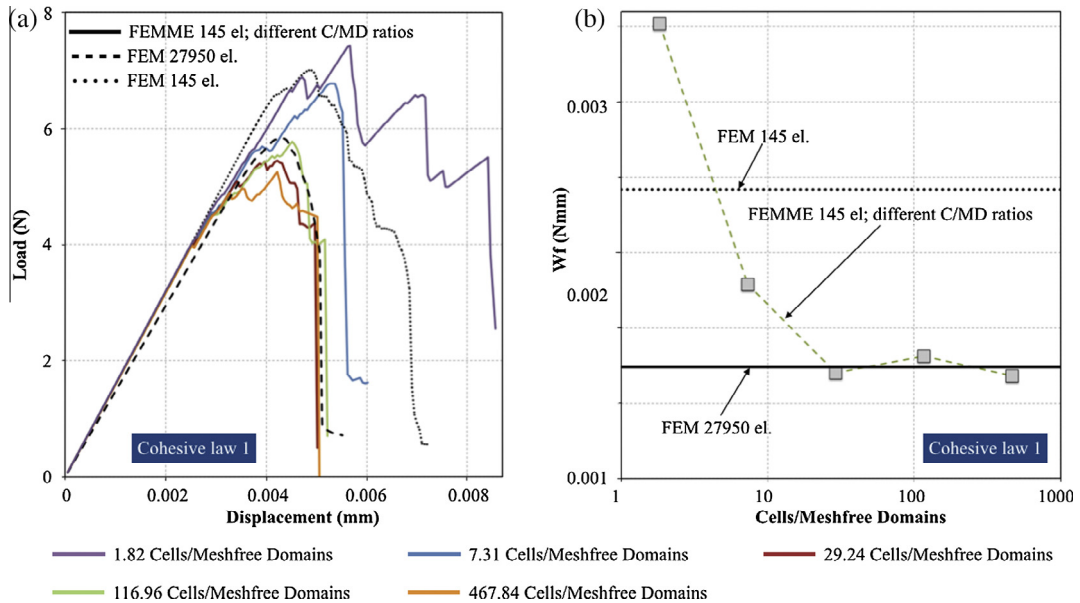


Fig. 15. Sensitivity analysis of the number of cells per Meshfree domain in the FEMME model: (a) load displacement curves, compared with the FEM; (b) work of fracture.

5. Validation C: Simulation of the size effect on strength of a concrete notched beam

In quasi-brittle materials, the fracture forms a discontinuous pattern of damage through its microstructure in the Fracture Process Zone (FPZ). This determines the fracture behavior of the structural element and causes the well-known size effect [20]; this has been widely studied numerically with continuous models [21–23]. In these models, which neglect the role of the microstructure, the fracture process zone is reproduced through the cohesive law that is defined for every element, which is essential to obtain quasi-brittle behavior [24]. As shown in Section 4, by using the FEMME methodology to insert the microstructure explicitly in the model, the cohesive law emerges. Hence it is not necessary to use a cohesive law to reproduce the effect of the FPZ in the global structure. The potential of this methodology to model the fracture process zone of a quasi-brittle material is shown in Fig. 17, which visualizes the formation of the crack front (red in the figure) in a model material with the following properties under a tensile load: elastic moduli, $E = 12$ GPa and $\nu = 0.2$; tensile strength,

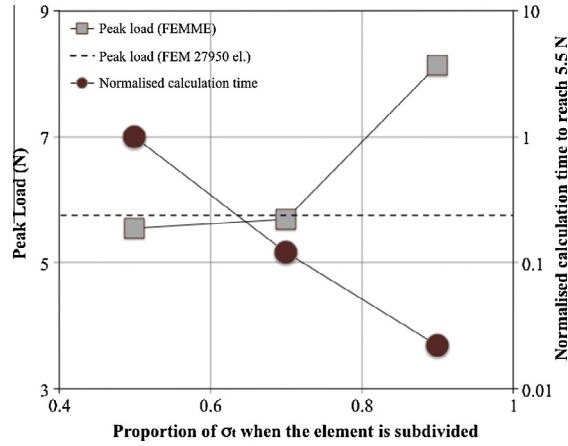


Fig. 16. Response of the model for different criteria of the subdivision initiation. Comparison of the peak load obtained and the computational cost normalized with the 0.5 case.

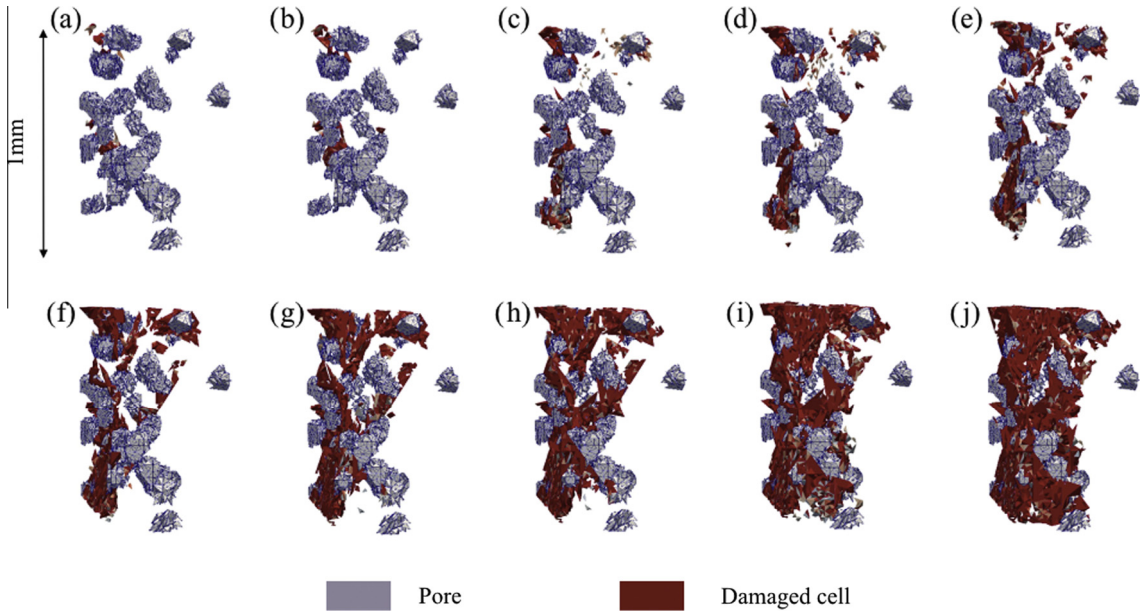


Fig. 17. Visualisation of crack formation in a quasi-brittle material under tension (the tensile stress is orthogonal to the image plane); the applied stress increases from (a) to (j). The damaged cells are plotted in red, and the cells of pores are shown in gray. (For interpretation of the references to color in this figure legend, the reader is referred to the web version of this article.)

$f_t = 3$ MPa; a porosity of 10% with a mean pore size of 0.1 mm and a standard deviation of 0.01 mm. In the sequence of images, damage starts forming between pores in different positions; these coalesce and grow to form the crack front, which begins to propagate.

The ability to reproduce explicitly the FPZ of a quasi-brittle material from its microstructural geometry and local properties makes the FEMME model capable of dealing with the size effect in structures formed by quasi-brittle materials, such as the concrete beams. Zhao et al. [25] performed a series of three point bending tests of concrete notched beams that show clearly the size effect. The beam dimensions are given in Table 1. The material properties of the concrete are: Young modulus of 39.2 GPa; Poisson's ratio of 0.2 and a tensile strength (f_t) of 4.5 MPa. The necessary data to model those beams with the FEMME method is in Table 1.

The fracture property of the cells in the FEMME simulation were defined using a critical strain that is equal to the tensile strength divided by the Young's modulus, and a final separation strain that is fitted as 3 times the critical strain. The properties of cells were defined randomly between these critical and final strains, assigned with a linear probability distribution as before. Due to the lack of information about the true microstructure of the material studied in [25], a synthetic

Table 1

Dimensions of the beams studied [25]: D is the total depth, N is the notch depth, S is the span and W is the width of the beam.

	D (mm)	N (mm)	S (mm)	W (mm)
Beam 1	400	160	800	120
Beam 2	200	80	800	120
Beam 3	150	80	600	120

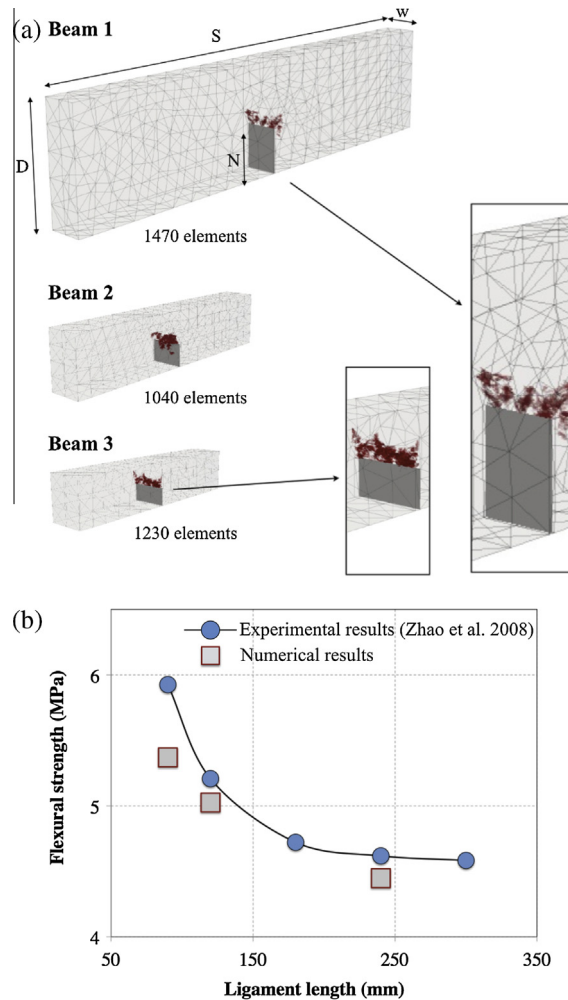


Fig. 18. Simulation of the fracture of concrete beams of different size: (a) The meshes used, which have similar discretization, and fracture patterns at the peak load (damaged cells shown in red) are illustrated; (b) comparison between the experimental results of Zhao et al. [25] and FEMME predicted peak loads. (For interpretation of the references to colour in this figure legend, the reader is referred to the web version of this article.)

microstructure is created for the beams with a porosity of 1%, formed by pores of an average size of 1 mm with a standard deviation of 0.2 mm. This microstructure neglects the effects of the aggregates and macropores in the concrete, but reproduces the micromechanical fracture processes that dominate the damage in the fracture process zone. In concrete the microporosity is mainly given by the bubbles in the water during the mixture [31]. The representative size of those pores is 1 mm, considered as entrained air if the size is smaller, and entrapped if its size is bigger. The development of damage in the 3 beams at peak load, simulated using the FEMME models with the same material and equivalent levels of discretization (i.e. similar FE mesh, cell size and microstructure), is shown in Fig. 18a; this reveals the fracture developed in each case is of similar length for the different ligament sizes. This determines the size effect, shown in Fig. 18b, which is consistent with the experimental results. The cohesive law, which commonly needs to be assumed in fracture modeling [26], is replaced by direct simulation of the damage that develops through the microstructure of the material. One possible way to explain the structural size effect [32] is the transference of stored volumetric elastic energy, to the surface fracture energy required by the fracture propagation process. This transfer of energy is consistent with our approach, since the stored volumetric energy

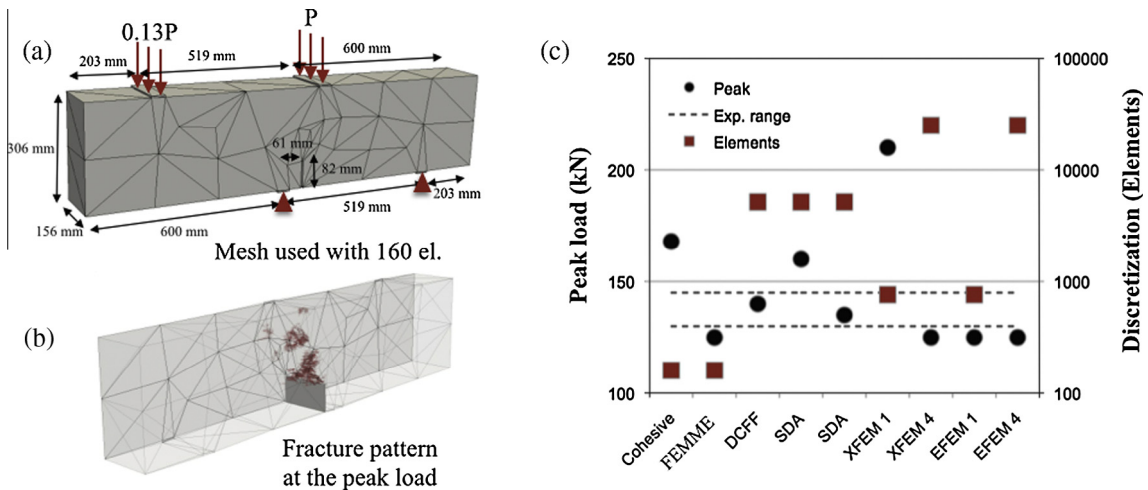


Fig. 19. Comparison between different methodologies; (a) mesh used in the FEMME model and its dimensions; (b) fracture pattern at the peak load of the FEMME model; (c) comparison of the peak load and discretization of the FEMME model and different numerical models based on FEM: Cohesive Elements, Cohesive Faces (DCFF) [28], Strong Discontinuities (SDA) [28], Nodal Enriched (XFEM 1, 4) [5] and Element Enrichment (EFEM 1, 4) [5].

released by the cells and then homogenized through the layers that provides the strain energy of the structure in the process of damage.

6. Validation D: Comparison with other enriched FE methodologies: 4 point shear simulation

Here we compare the FEMME method with other methodologies that are typical used in computational fracture mechanics, of which E-FEM and X-FEM [5] are example enrichment methodologies that can also reach a good solution with a coarse mesh; these require the assumption of a cohesive law. The release of the spurious fracture energy in the FEMME methodology is equivalent to that achieved by E-FEM. To show this, we simulate the four point shear test carried out by Arrera and Ingraffea [27], which is a common benchmark test for numerical fracture models. We compare the FEMME simulation results with the numerical models of Oliver et al. [5] and Yu et al. [28]; all were applied to this same problem, with the geometry and material properties described by Arrera and Ingraffea [27]. The FE mesh used, with 160 tetrahedral elements with a single integration point, is shown in Fig. 19a; fracture is defined at the peak load. The average volume of the cells introduced in the FEMME model is 1 mm^3 . The material properties used are: elastic moduli, $E = 24.8 \text{ GPa}$, Poisson's ratio 0.2; tensile strength $f_t = 2.8 \text{ MPa}$; and a final strain for the cells arbitrarily chosen as 3 times the critical strain, which is f_t/E . The synthetic microstructure created has a porosity of 1%, which is formed by pores of an average size of 1 mm with a standard deviation of 0.2 mm. Comparison is made Fig. 19b, in terms of the predicted fracture load (data for the range of strength experimentally measured by Arrera and Ingraffea [27] are shown) and the number of elements, with other methodologies that either need to predefine a fine mesh along the fracture path, such as Cohesive Faces (DCFF) [2], cohesive elements [3] or strong discontinuities (SDA) [28], and those that can deal with a mesh without a predefined fracture path, such as XFEM and EFEM [5]. The FEMME model is shown to reach a good solution using a coarse mesh, demonstrating the potential for this methodology to simulate fracture using the coarse mesh in structural elements without requiring a predefined fracture path.

7. Conclusion

Through the multi-scale application of Meshfree and Cellular Automata models, we have demonstrated a novel Finite Element Microstructure MESHfree (FEMME) method of conducting a normalization of the energy release of a Finite Element Method calculation with a coarse mesh. This allows us to carry out, with significant efficiency, FE calculations of strain development with a coarse mesh without losing accuracy in the solution. This is achieved through a high fidelity reproduction of the microstructure and the adaptation of the Meshfree Model to its geometry. Importantly, the computational cost of the FEMME method is lower than a FEM with a similar discretization. This makes the FEMME model very promising for the fracture modeling of components at engineering scale, taking into account the effects of the microstructure of the material.

Acknowledgement

This work was carried out within the UK EPSRC project "QUBE: Quasi-Brittle fracture: a 3D Experimentally-validated approach" (EP/J019992/1).

Appendix A. Supplementary material

Supplementary data associated with this article can be found, in the online version, at <http://dx.doi.org/10.1016/j.engfracmech.2015.05.059>.

References

- [1] Yang Z, Ren W, Mostafavi M, McDonald SA, Marrow TJ. Characterisation of 3D fracture evolution in concrete using in-situ X-ray computed tomography testing and digital volume correlation. In: Proceedings of the 8th international conference on fracture mechanics of concrete and concrete structures FraMCoS; 2013. p. 236–242.
- [2] Yu RC, Saucedo-Mora L, Ruiz G. Finite element study of the diagonal tension failure in reinforced concrete beams. *Int J Fract* 2011;169(2):169–82. <http://dx.doi.org/10.1007/s10704-011-9592-z>.
- [3] Ortiz M, Pandolfi A. Finite deformation irreversible cohesive elements for three dimensional crack propagation analysis. *Int J Numer Methods Eng* 1999;44:1267–82. [http://dx.doi.org/10.1002/\(SICI\)1097-0207\(19990330\)44:9<1267::AID-NME486>3.0.CO;2-7](http://dx.doi.org/10.1002/(SICI)1097-0207(19990330)44:9<1267::AID-NME486>3.0.CO;2-7).
- [4] Oliver J. Modelling strong discontinuities in solid mechanics via strain softening constitutive equations. Part 1: Fundamentals. *Int J Numer Meth Engng* 1998;39(21):3575–600. [http://dx.doi.org/10.1002/\(SICI\)1097-0207\(19961115\)39:21<3575::AID-NME65>3.0.CO;2-E](http://dx.doi.org/10.1002/(SICI)1097-0207(19961115)39:21<3575::AID-NME65>3.0.CO;2-E).
- [5] Oliver J, Huespe AE, Sánchez PJ. A comparative study on finite elements for capturing strong discontinuities: E-FEM vs X-FEM. *Comput Methods Appl Mech Eng* 2006;195:4732–52. <http://dx.doi.org/10.1016/j.cma.2005.09.020>.
- [6] Chakraborty A, Rahman S. Stochastic multiscale models for fracture analysis of functionally graded materials. *Engng Fract Mech* 2008;75:2062–86. <http://dx.doi.org/10.1016/j.engfracmech.2007.10.013>.
- [7] Shterenlikht A, Howard IC. The CAFE model of fracture-application to a TMCR steel. *Fatigue Fract Engng Mater Struct* 2006;29(9–10):770–87. <http://dx.doi.org/10.1111/j.1460-2695.2006.01031.x>.
- [8] Talebi H, Silani M, Bordas SPA, Kerfriden P, Rabczuk T. A computational library for multiscale modelling of material failure. *Comput Mech* 2013;53(3):1047–71. <http://dx.doi.org/10.1007/s00466-013-0948-2>.
- [9] Saucedo-Mora L, Marrow TJ. Method for the explicit insertion of microstructure in Cellular Automata Finite Element (CAFE) models based on an irregular tetrahedral Finite Element mesh: application in a multi-scale Finite Element Microstructure Meshfree framework (FEMME). *Finite Elements Anal Des* 2015 [submitted for publication].
- [10] Saucedo-Mora L, Marrow TJ. 3D cellular automata finite element method to model quasi-brittle fracture. In: Twelfth international conference on engineering structural integrity assessment conference proceedings, ESIA 2013, Manchester, EMAS Publishing; 2013.
- [11] Hill R. On the micro-macro transition in constitutive analysis of elastoplastic response at finite strain. *Math. Proc. Camb. Phil. Soc.* 1985;98:579–85. <http://dx.doi.org/10.1017/S0305004100063787>.
- [12] Lee DT, Schachter BJ. Two algorithms for constructing a Delaunay triangulation. *Int J Comput Inform Sci* 1980;9(3):219–41. <http://dx.doi.org/10.1007/BF00977785>.
- [13] Arroyo M, Ortiz M. Local maximum-entropy approximation schemes: a seamless bridge between finite elements and meshfree methods. *Int J Numer Methods* 2006;65:2167–202. <http://dx.doi.org/10.1002/nme.1534>.
- [14] Saucedo Mora L. Meshfree methods applied to tensile fracture and compressive damage in quasi-brittle materials. Ph.D. Thesis, University of Castilla-La Mancha, Spain; 2012.
- [15] Fries TP, Matthies HG. Classification and overview of meshfree methods. Brunswick, Germany: Institute of Scientific Computing, Technical University Braunschweig; 2004.
- [16] Slabaugh G. Computing Euler angles from a rotation matrix. Retrieved on August 6; 1999. p. 10.
- [17] Belytschko T, Chen JS. Meshfree and particle methods. Blackwell: Wiley; 2003 [ISBN-13: 978-0470848005].
- [18] Saucedo-Mora L, Mostafavi M, Khoshkhou D, Reinhard C, Atwood R, Zhao S, et al. Simulation by cellular automata finite elements (CAFE) in a Microstructural Adaptive Meshfree framework (MAM) of indentation damage in a SiC–SiC fibre ceramic matrix composite. *J Mech Phys Solids* 2014 [submitted for publication].
- [19] Saucedo-Mora L, Slamecka K, Thandavamoorthy U, Marrow TJ. Multi-scale modelling of the effect of the bond coat roughness on damage development in a (plasma-sprayed) thermal barrier coating. *Surf Coat Technol* 2015 [submitted for publication].
- [20] Bažant ZP, Asce F. Size effect in blunt fracture: concrete, rock and metal. *J Eng Mech* 1984;110(4):518–35 [ISSN 0733-9399/84/0004-0518/].
- [21] Saucedo-Mora L, Yu RC, Ruiz G. Fully-developed FPZ length in quasi-brittle materials. *Int J Fract* 2012;178(1–2):97–112. <http://dx.doi.org/10.1007/s10704-012-9769-0>.
- [22] Ooi ET, Yang ZJ. Efficient prediction of deterministic size effect using the scaled boundary finite element method. *Engng Fract Mech* 2010;77(6):985–1000. <http://dx.doi.org/10.1016/j.engfracmech.2010.01.002>.
- [23] Haidar K, Pijaudier-Cabot G, Dubé JF, Loukili A. Correlation between the internal length, the fracture process zone and size effect in model materials. *Mater Struct* 2005;38(2):201–10. <http://dx.doi.org/10.1007/BF02479345>.
- [24] Bažant ZP, Planas J. Fracture and size effect in concrete and other quasi-brittle materials. CRC Press; 1997 [ISBN-10:084938284X].
- [25] Zhao Z, Kwon SH, Shah SP. Effect of specimen size on fracture energy and softening curve of concrete: Part I. Experiments and fracture energy. *Cem Concr Res* 2008;38(8–9):1049–60. <http://dx.doi.org/10.1016/j.cemconres.2008.03.017>.
- [26] Mostafavi M, Baimpas N, Tarleton E, Atwood RC, McDonald SA, Korsunsky AM, et al. Three-dimensional crack observation, quantification and simulation in a quasi-brittle material. *Acta Mater* 2013;61:6276–89.
- [27] Arrea M, Ingraffea AR. Mixed-mode crack propagation in mortar and concrete. Report n° 81–13: Department of Structural Engineering, Cornell University; 1982.
- [28] Yu RC, Ruiz G, Chaves EWW. A comparative study between discrete and continuum models to simulate concrete fracture. *Engng Fract Mech* 2008;75(1):117–27. <http://dx.doi.org/10.1016/j.engfracmech.2007.03.031>.
- [29] Carpinteri A, Colombo G. Numerical analysis of catastrophic softening behavior (snap back instability). *Comput Struct* 1989;31:607–36. [http://dx.doi.org/10.1016/0045-7949\(89\)90337-4](http://dx.doi.org/10.1016/0045-7949(89)90337-4).
- [30] Möes N, Belytschko T. Extended finite element method for cohesive crack growth. *Engng Fract Mech* 2002;69:813–33. [http://dx.doi.org/10.1016/S0013-7944\(01\)00128-X](http://dx.doi.org/10.1016/S0013-7944(01)00128-X).
- [31] Proceedings of the 9th FIB International PhD Symposium in Civil Engineering; 2012.
- [32] Bažant ZP. Size effect. *Int J Solids Struct* 2000;37:69–80.